All-Optical Synapse With Directional Coupler Structure Based on Phase Change Material

Yong Zhang, Danyang Yao, Yan Liu, Cizhe Fang, Shulong Wang, Guosheng Wang, Yan Huang, Xiao Yu, Genquan Han, *Member, IEEE*, and Yue Hao, *Senior Member, IEEE*

***Abstract*—With the rapid growth of the artificial neural network, the operational efficiency of von Neumann computing architecture is limited by the separation of memory and processor, and the exploration of the efficient hardware mimicking bionic neurons and synapses has become a matter of great urgency. Moreover, the circuit implements for this architecture have potential limitations such as slow switching speed, high computational power consumption, and high interconnection loss. As an alternative, neuromorphic engineering in the photonic domain has recently gained widespread international attention. In this work, we propose an all-optical synaptic device based on a directional coupler structure, which can control the degree of light field distribution variation by changing the state of the phase change material $Ge_2Sb_2Te_5$ (GST) distributed in discrete islands on one port. The mode distribution and propagation of the field have been carefully analyzed with pulsed light of different power. More importantly, it is possible to flexibly design the weight update of the synaptic devices by varying the size and location of the GST islands. Verified by the Spiking Neural Network, we can improve the recognition accuracy of handwritten figures from the original 50% to 91% by improving the linearity and accuracy of the synapse weights. This may provide a new solution for future low-power non-volatile photonic integrated circuits.**

***Index Terms*—Directional coupler, photonic integrated circuits, synaptic device, weight linearity.**

I. Introduction

To meet the needs of efficient data processing in the era of big data, neuromorphic computing provides a breakthrough that could try to replace the existing Von Neumann computing [1]. Unlike traditional computing systems where the central computing unit is separated from the main memory, each neuron in the human brain acts as an independent computing and memory unit. This computing system is superior in efficiency and lower in power consumption compared to classical computing system [2]. Therefore, a new type of neuromorphic device that can process and record data at the same time is needed to complete calculations similarly to the human brain [3].

Among rapidly changing neuromorphic devices, electronic computing cannot meet the demand for the rapid growth of computing speed and information-carrying capacity brought about by emerging applications such as big data, machine learning and artificial intelligence, and therefore optical computing has become one of the promising solutions [4], [5]. Programmable photonic elements and nonlinear elements are indispensable components in optical computing [6], and phase change materials (PCM), such as $Ge_2Sb_2Te_5$ (GST), is one of the ideal materials for realizing optical programmable [7]–[9]. The optical properties of GST can be significantly different in crystalline(c-GST) and amorphous (a-GST) states, which can be transformed by electrical or optical methods [10], [11]. Compared with electro-optic modulation and thermos-optic modulation methods, the non-volatility, which means that no power source or light source is needed to maintain the programming state and store information, enables the devices using GST to have the advantage of low power consumption [7], [12], [13]. Silicon optoelectronics has long been the mainstream of nowadays optical neuromorphic devices for its compactness and compatibility with a traditional CMOS process, and however, silicon-based optoelectronic devices encounter their intrinsic bottleneck due to the limited refractive index tuning range in this flourishing age of artificial intelligence [14], [15]. Silicon based photonic devices using GST materials with extremely large refractive index tuning range have been reported to address this issue, such as Mach–Zehnder interferometers (MZI) structures [16]–[18], micro-ring resonators [19]–[22], optical switches [23], [24], directional couplers [25]–[27]and some other devices [28]–[30]. However, all-silicon optical synaptic devices using GST materials have a non-negligible problem of nonlinear weight update. An ideal synaptic device should assume to behave with a strictly linear update of the weight under the input stimulus. The linearity of the weight update of the synaptic device has a great impact on the recognition accuracy of the neural network [31], [32]. However, in reality, this assumption may not hold [33]. It has been reported

Manuscript received June 24, 2021; revised July 26, 2021; accepted July 31, 2021. Date of publication August 4, 2021; date of current version August 23, 2021. This work was supported by the National Key Research and Development Project under Grant 2018YFB2202800, in part by the National Natural Science Foundation of China under Grants 62004145, 61534004, 91964202, 61874081, and 61851406, and in part by the Major Scientific Research Project of Zhejiang Lab under Grant 2021MD0AC01. *(Corresponding authors: Danyang Yao; Yan Liu.)*

Yong Zhang, Danyang Yao, Yan Liu, Cizhe Fang, Shulong Wang, Guosheng Wang, Yan Huang, and Yue Hao are with the State Key Discipline Laboratory of Wide Band Gap Semiconductor Technology, School of Microelectronics, Xidian University, Xi'an 710071, China (e-mail: yzhang_7@126.com; dyyao@xidian.edu.cn; xdliuyan@xidian.edu.cn; 513864504@qq.com; slwang@xidian.edu.cn; gswangxd@163.com; hy04131432@126.com; yhao@xidian.edu.cn).

Xiao Yu is with the Research Center for Intelligent Chips, Zhejiang Lab, Hangzhou 311121, China (e-mail: yuxiao@zhejianglab.com).

Genquan Han is with the State Key Discipline Laboratory of Wide Band Gap Semiconductor Technology, School of Microelectronics, Xidian University, Xi'an 710071, China, and also with the Research Center for Intelligent Chips, Zhejiang Lab, Hangzhou 311121, China (e-mail: hangenquan@gmail.com).

Digital Object Identifier 10.1109/JPHOT.2021.3102132

This work is licensed under a Creative Commons Attribution 4.0 License. For more information, see https://creativecommons.org/licenses/by/4.0/

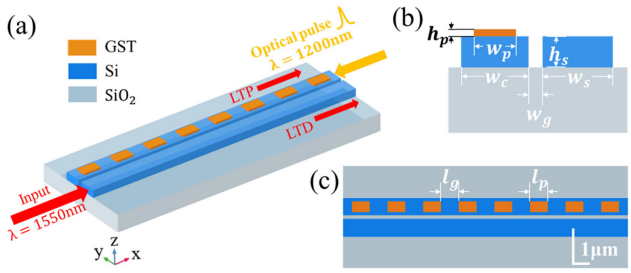


Fig. 1. The structure diagram of the designed all-optical synapse device. (a) The 3D structure of the all-optical synaptic device. (b) Cross-sectional view of the device at the GST island location. (c) The top view of the device.

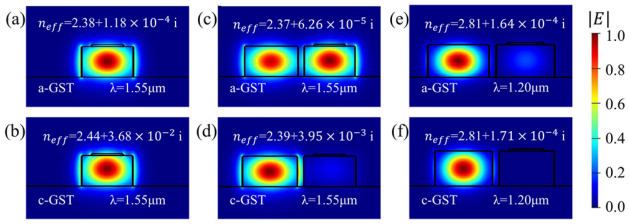


Fig. 2. Waveguide mode analysis. Normalized electrical field profiles of the TE mode at 1550 nm in a waveguide with GST in the (a) amorphous and (b) crystalline state. The waveguide with a width of 480 nm is combined with a 10 nm-thick-GST film. Normalized electrical field profiles in the two-waveguide system when the GST is in (c) (e) amorphous and (d) (f) crystalline state. The widths of the waveguide combined with GST and the empty waveguide are w_c =480 nm and w_s =500 nm, respectively. The modes are simulated for TE polarization at (c-d) 1550 nm and (e-f) 1200 nm respectively.

that an all-optical neuro synaptic device is realized by superimposing island-like distributed GST materials on the waveguide [22], [34]. However, the synaptic weights of these designs are fixed, which results in the lack of improved accuracy and flexibility.

In this article, we propose an all-optical synaptic device based on a directional coupler structure. The island-shaped phase-change material GST is superimposed on an optical path of the directional coupler, and the degree of light exchange is controlled by changing the number of amorphous islands of the GST material. The solution of adjusting the number of amorphous islands by pulsed light is verified by photo-thermal coupling simulations. The all-optical synapse device based on the directional coupler structure we proposed can realize the functions of long-term potentiation (LTP) and long-term depression (LTD) at the same time. More importantly, the weight update of the device can be more linearized by adjusting the position and size of the GST islands. Through the verification in the Spiking Neural Network (SNN), the recognition accuracy of the device after linear correction can be improved compared with that without correction. Such powerful functions and flexible weight adjustment make this novel all-optical synaptic device an excellent candidate for bionic synapses and on-chip photonics.

II. Device Structure and Theory Analysis

Fig. 1 shows the structure of an optical synaptic device. Eight islands of phase change material GST arrays are distributed on the surface of an optical waveguide of the directional coupler. The state of these GST islands can be changed by applying light pulses to one port to change the synapse weight. As shown in Fig. 1(a), the basic structure of the device is a 1×2 directional coupler, with an input port and two optical output ports. Since these two output ports can respectively realize the LTP and LTD functions of the synaptic device, they are defined as LTP ports and LTD ports. Fig. 1(b) shows the cross-sectional schematic of the device with the GST islands on the left. The width w_s of the waveguide without GST islands is 500 nm, and the waveguide with GST islands has the width w_c of 480 nm. For coupling, the waveguide height h_s takes a typical value of 220 nm based on a commercial SOI wafer. The principle of the device is to partially couple light from the input port to the output port. To reduce the optical attenuation due to the absorption of crystalline GST and the footprint of the device, the coupling length should be reduced as much as possible in the design, so the value of w_g in this article is 60 nm. To make sure the state transition of GST realistically, the width w_p is 300 nm, and the height h_p is 20 nm. Both the island length l_p and the island gap l_g are 1000 nm. The coupling length and the size of the GST islands together determine the number of GST islands, which is eight, as shown in the top view of the device in Fig. 1(c).

Initially, all the eight GST islands remain crystalline. Since the GST island distribution in the designed structure is not uniform, the average effective refractive index method is used to approximate them when conducting mode analysis on the waveguide. As mentioned above, the thickness of the GST islands is 20 nm. Since the length and gap of the GST islands are both 1000 nm, the average GST thickness used in the mode analysis is 10 nm simply. As shown in Fig. 2(a), when the waveguide width is 480 nm, the real part of the effective refractive index of the waveguide combined with amorphous GST is 2.38, which is closest to that of the 500 nm-wide waveguide without GST islands, which results in the optimal coupling effect illustrated in Fig. 2(c). The refractive indices of the materials are taken as $\mathrm{n_{Si}} = 3.481$, $\mathrm{n_{SiO2}} = 1.445$, $\mathrm{n_{a-GST}} = 3.9027 + 0.0055\mathrm{i}$ and $\mathrm{n_{c-GST}} = 6.0769 + 0.9040\mathrm{i}$ [35]. According to the theory of coupling mode, to achieve efficient coupling, the two waveguides need to have the same or similar mode propagation constants. When the GST islands are crystalline, the real part of the effective refractive index of the single waveguide combined with the GST islands is 2.44, which cannot be effectively coupled with the 500 nm-wide waveguide, as shown in Fig. 2(d). In the case of this phase mismatch, the mode power in the two waveguides cannot be effectively exchanged. Through mode analysis, the coupling length of this structure can be optimized theoretically as 16um.

In the input port, the incident light of 1550 nm is introduced from the input port. However, if the pulsed light of 1550 nm is introduced as a stimulus for GST islands from the LTP port, the pulsed light will inevitably be coupled into another waveguide due to the amorphous state of the few GST islands, as shown in Fig. 2(c). To localize the pulsed light in the GST islands to reduce optical loss, a wavelength of 1200 nm is chosen. At this wavelength, no matter whether the GST islands

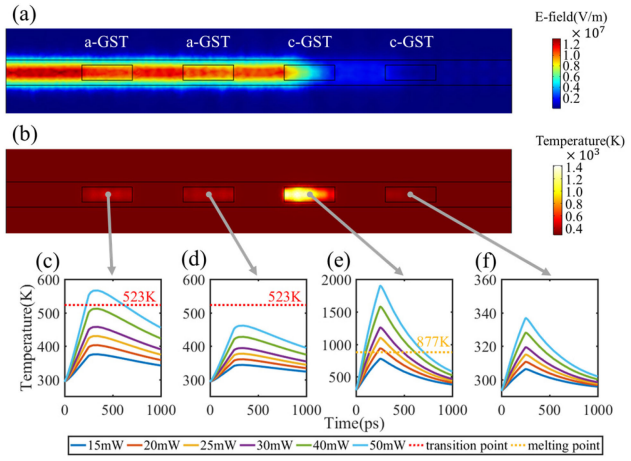


Fig. 3. The island state transition scheme. The model in the figure is a Si waveguide combined with four GST islands, in which the first two are amorphous GST and the latter two are crystalline GST. The main purpose is to verify that crystalline GST islands can be transformed into amorphous one by one. (a) The optical field distribution in the waveguide at 30 mW input light. (b) The temperature distribution after a light pulse with a power of 30 mW for 250 ps. (c)–(f) The temperature changes of the center positions of the four GST islands corresponding to Fig. (b) under different power light pulses. The light pulse width is 250 ps.

are crystalline or amorphous, the two waveguides will not be remarkably coupled, as shown in Fig. 2(e) and (f). When all GST islands are amorphous, 83% of the light can be localized in the GST-combined waveguide without being coupled into the other waveguide. What's more, compared with the pulsed light of 1550 nm, the crystalline GST material has a stronger light absorption for 1200 nm, which is beneficial to transform the crystalline GST islands into an amorphous state by heating to the melting temperature.

III. Results and Discussion

The whole transforming process of the state of GST islands can be analyzed using Finite Element Method (FEM) in commercial COMSOL Multiphysics software [36]. The simplified model was built as four GST islands distributed on a silicon waveguide, in which the first two islands are amorphous, and the second two islands are crystalline. In this simulation, the optical power absorbed by the material due to the imaginary part of the refractive index will be converted into heating power, which is used to simulate the state transition of the GST islands. Fig. 3(a) shows the light field distribution of this model with pulsed light of 30mV. It shows that most light passes through all the first three islands (including two amorphous islands and one crystalline island), however, it is mostly absorbed by the third GST island due to the huge difference between the absorption coefficients of crystalline and amorphous states. Fig. 3(b) shows the temperature distribution for these four GST islands after a 30 mW light pulse for 250 ps, which exhibits the highest temperature for the third island predicted by Fig. 3(a) under "writing" speed of sub-ns orders. Then the variation of the temperature along the central line of four GST islands after injecting light pulses with different power was compared in Figs. 3(c)-(f). When choosing the proper power range between 20 mW to 40 mW, the third GST island all can be heated beyond the melting temperature (877K), which results in a transition to an amorphous state. In the meanwhile, during such a power range the first two amorphous GST islands remain below the key transition temperature (523K), at which they can transit from the amorphous state to the crystalline state. This proves the rationality of the tuning scheme of weight adjustment we proposed, that is, pulsed light with proper power can transform the GST island state into an amorphous state one by one. We can use the electrical means of electrically heating the substrate part[37] or the optical means of irradiating the laser from the top to heat the GST islands to the transition temperature (523K), so as to transform all the GST islands into a crystalline state and realize the weight initialization.

In the directional coupler, the distribution of light power in the two waveguides versus the position of the waveguide is as follows:

$$P_1 = P_0 \left[\sin\left(\frac{\pi x}{2L_c}\right)\right]^2 \tag{1}$$

and

$$P_2 = P_0 \left[\cos\left(\frac{\pi x}{2L_c}\right)\right]^2 \tag{2}$$

where P_1 is the light power distribution in the waveguide to be coupled, P_2 is the light power distribution in the waveguide of the input light wave, P_0 is the input port power, and L_c is the optimal coupling length, which means that the light energy fully enters the desired waveguide to be coupled.

The length of the coupling region of the two waveguides is controlled by the number of islands of amorphous GST, so the region of amorphous GST islands is the effective coupling region. In this way, the output light power of the two output ports can be controlled. The output power of the two ports are:

$$P_{LTP} = \left[P_{in} - \alpha_c \left(L_c - L_e\right)\right] \left[\sin\left(\frac{\pi L_e}{2L_c}\right)\right]^2 \tag{3}$$

and

$$P_{LTD} = \left[P_{in} - \alpha_c \left(L_c - L_e\right)\right] \left[\cos\left(\frac{\pi L_e}{2L_c}\right)\right]^2 \tag{4}$$

where P_{LTP} and P_{LTD} are the light power of LTD and LTP output ports, respectively, P_{in} is light power of the input port, α_c is the light loss per unit length generated at the crystalline GST island due to light absorption of the crystalline GST material, L_e is the effective coupling length. The optical loss in the amorphous GST island region is ignored in the model.

The optical response of an optical synaptic device was obtained using a commercial-grade simulator Lumerical FDTD Solutions based on the finite-difference time-domain (FDTD) method [38]. The initial state is that all GST islands are in the crystalline state, that is, the effective coupling length $L_e = 0$. The optical power of the LTP port is the least, and the synapse weight for this port is the smallest. The LTD port has the largest optical power, and the synapse weight for this port is the largest. The change of synapse weight can be achieved by changing

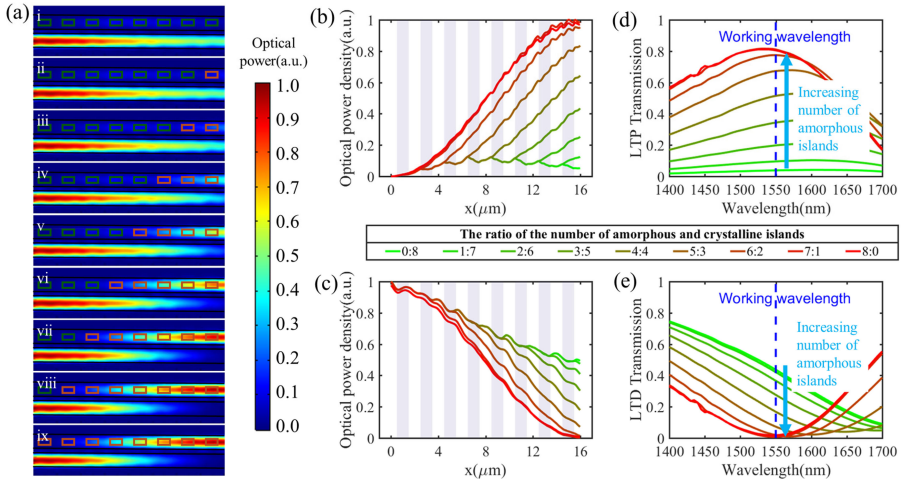


Fig. 4. FDTD simulation results (a) Optical power distribution inside the all-optical synaptic device with eight GST islands on top. (i to ix). Initially, all GST islands are in the crystallized state (i, green boxes). Subsequently, 1 (ii), 2 (iii), 3 (iv), 4 (v), 5 (vi), 6 (vii), 7(viii), 8(ix) islands are gradually amorphous (orange boxes). The electric field distribution along the centerline of (b) the LTP port waveguide and (c) the LTD port waveguide, respectively. The gray area is the location of the GST islands. The power of the light waves at the normalized (d) LTP output port and (e) LTD output port varies with the number of crystalline GST islands. (d) LTP and (e) LTD port transmission characteristics with the increasing number of amorphous islands. The blue dotted line marks the designed working wavelength of 1550 nm. As the number of amorphous islands increases, transmission at the LTP (LTD) port increases (decreases) thus realizing positive (negative) integration action of the neuron.

the crystalline GST islands to the amorphous state one by one, which can be controlled by the pulsed light that enters the GST-combined waveguide from the LTP port. Injecting from the right LTP port, the already-transited amorphous GST islands can have minimal power exchange with the rest of crystalline islands, which have comparatively larger absorption coefficients. In the process of changing GST islands' states one by one, the effective coupling length L_e gradually increases with the increase of the number of amorphous islands. According to formulas (3) and (4), the optical power of the LTP port gradually increases, while the optical power of the LTD port gradually decreases, which achieves the adjustment of the synaptic weight.

The whole transition process after injection of pulsed light from the LTP output is shown in Fig. 4(a). It could be seen that when the GST islands are transformed into an amorphous state one by one, the effective coupling length gradually increases, and the light energy of the two output ports gradually increases and decreases, respectively corresponding to the LTP and LTD function in the optical nerve synapse device. Fig. 4(b) and (c) respectively show the power distribution in the waveguides corresponding to the LTP and LTD output ports during the whole transition process. The gray area is the location of the GST islands. It could be seen from the figures that the power distribution in the waveguide changes at every beginning of the GST islands. This is consistent with our design, which is the number of crystalline GST islands controls the effective coupling length, thereby controlling the optical power of the output port. Fig. 4(d) and (e) show that the transmission of the LTP and LTD output ports changes with wavelength with different numbers of amorphous GST islands, corresponding to different weights of the synaptic device. As the number of amorphous islands increases, transmission at the LTP (LTD) port increases (decreases) monotonically, thus realizing positive (negative) integration of the synapse at the working wavelength of 1550 nm. Therefore, the wavelength beyond 1550 nm is neglected for its monotony of chaos, which can be attributed to the gradually destroyed mode matching between two adjacent waveguides for longer wavelengths.

TABLE I
THE LENGTH DIMENSION AND CENTER POSITION OF EACH GST ISLAND IN THE FOUR DESIGNS

Device	Length (μm)	Central position (μm)							
Original 9 levels	1.00	1.00	3.00	5.00	7.00	9.00	11.00	13.00	15.00
Linear 9 levels	1.00	1.81	4.51	6.02	7.35	8.65	9.98	11.49	14.19
original 20 levels	0.50	0.80	1.60	2.40	3.20	4.00	4.80	5.60	6.40
		7.20	8.00	8.80	9.60	10.40	11.20	12.00	12.80
		13.60	14.40	15.20					
Linear 20 levels	0.50	1.18	2.86	3.76	4,51	5.17	5.78	6.36	6.92
		7.46	8.00	8.54	9.08	9.64	10.22	10.83	11.49
		12.24	13.14	14.82					

Furthermore, the variation of the synapse weight can be achieved by adjusting the size and distribution of the GST islands. Accordingly, we anticipate that the accuracy and linearity of synaptic weights can be improved by the island distribution and the number of islands. The specific design parameters are shown in Table I The simulation result of synapse weight before and after correction is shown in Fig. 5. Fig. 5(a) shows the top view of the two devices with different islands before and after the correction. It is necessary to ensure that pulse energy that stimulates the GST island state change is consistent, so the island size needs to be consistent in each design. Here we only tune the distribution by changing the location of the islands. In the original 9-level synaptic devices, the GST islands are all 1000 nm in length and are evenly distributed. It can be seen from Figs. 5(b) that the normalized transmission of this original design is very poor in linearity. According to the formulas (3) and (4), the weight distribution for this normalized transmission

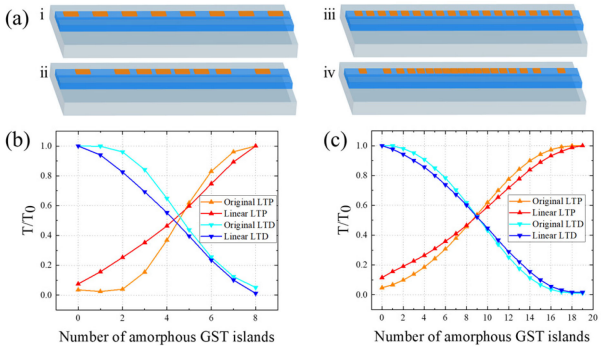


Fig. 5. Simulation results of improvement. (a) Changes in device structure before and after improvements. The main changes are the size and location of the GST islands. The device structure of (i) original 9 levels, (ii) linear 9 levels, (iii) 20 levels with evenly distributed islands, and (iv) linear 20 levels. Normalized transmission characteristics of (b) 9-level devices and (c) 20-level devices vary with the number of amorphous islands, i.e., the synapse weight varies with the number of pulses.

is characterized by a steep slope of the tangent in the middle and small slopes of the tangent on both ends, which is associated with the nonlinear change for the effective coupling length L_e in the evenly spaced distribution. To enhance the linearity of the normalized transmission, the islands in the middle should have a smaller space and the islands on both ends should have a larger space, which consists with the nonlinear effective coupling length L_e predicted by the formulas (3) and (4) accordingly. The 9-level design after linear correction behaves more linearly as shown in Figs. 5(b) both for the LTP and LTD ports. In addition, the accuracy of synaptic weights also can be further improved by changing the size of the islands, besides changing the position of the islands to correct the linearity. The length of the islands on the device with 20 levels of synaptic weight is reduced to 500 nm. Its design principle of linear correction follows the same principle as the above, which also exhibits noticeable advantages in linearity in Figs. 5(c) both for the LTP and LTD ports. We use the residual sum of square of linear fitting to evaluate linearity. The linearity of the LTP function of the 9-level devices was improved from 0.087 to 0.007, and the linearity of the LTD function was improved from 0.052 to 0.008. The LTP and LTD linearity of the 20-level devices were improved from 0.055 and 0.084 to 0.015 and 0.038, respectively.

A new all-optical neural network unit is proposed based on the above simulation, as shown in Fig. 6. The unit consists of two all-optical synaptic devices. One of them increases the positive synaptic output and weakens the negative synaptic output after receiving the positive stimulus pulse light. The other makes the positive synaptic output weaken and the negative synaptic output increase after receiving the negative stimulation pulse light. This approach not only makes the weight of a synaptic device can be reversibly tuned by alternate LTP and LTD operations, but also achieves two opposite synaptic outputs, which means that while enhancing or inhibiting one synapse, the other synapse is reversely regulated.

To evaluate the performance of the synapse, a three-layer fully connected Spiking Neural Network (SNN) based on Leaky Integrate and Fire (LIF) model is used to recognize handwritten

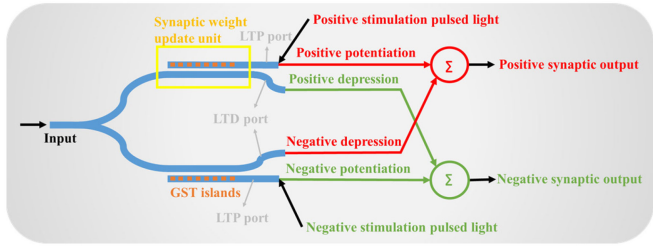


Fig. 6. A new all-optical neural network unit. The unit consists of two all-optical synaptic devices. Positive stimulation pulse light adjusts the weight of the upper device, which in turn increases the positive synaptic output and weakens the negative synaptic output. The same is true for negative stimulation pulsed light.

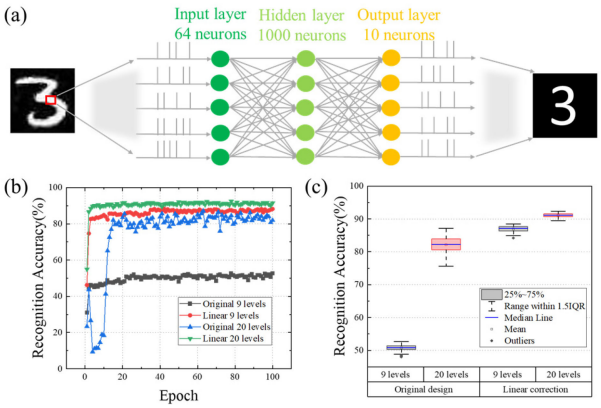


Fig. 7. (a) Three-layer fully connected Spiking Neural Network based on LIF model. (b) Simulated Convolutional SNN's learning accuracy evolution based on four all-optical synaptic devices. (c) Statistical graph of learning accuracy between 20 and 100 epochs. Accuracy above 90% can be achieved in SNN based on all-optical synaptic devices by varying the device linearity and accuracy.

figures, as shown in Fig. 7(a). Each pixel of a handwritten figure image is divided into a stream of spikes whose frequency is proportional to the pixel intensity. Through several synapses between the three layers of neurons (input layer, hidden layer, and output layer), handwritten figures can be recognized. Fully connected networks involve a series of neuron layers between the input and the output layers. The output of each neuron in a layer is connected to the inputs of all the neurons in the subsequent layer [39]. The neuron state is determined by the neuron state of the previous level and the synapse weight between the two levels of neurons. Mathematically, this can be represented to the formula [22]:

$$V_{\mathrm{j[t]}} = V_{\mathrm{j[t-1]}} + \sum_i I_{i[t]} w_{ij} \tag{5}$$

where $V_{\mathrm{j[t]}}$ is the internal state of the $\mathrm{j^{th}}$ neuron at time t, $I_{i[t]}$ is the $\mathrm{i^{th}}$ input at time t, w_{ij} is the weight of the synapse connecting the $\mathrm{i^{th}}$ input to the $\mathrm{j^{th}}$ neuron. The synapse weight data in the SNN corresponds to the device data in Fig. 5 in a table look-up manner. Learning accuracy evolution is shown in Fig. 7(b). It can be seen that the recognition accuracy of the original 9 level synaptic device is only 50%. After linear correction, it can be increased to 87%. In addition, increasing the number of synaptic weights to 20 level can further improve the recognition

accuracy to more than 80%, but it is comparably inferior due to the remarkable prolonged training time. Finally, optimizing the linearity and the number of levels at the same time can increase the recognition accuracy to 91%, which implies that there lies a tradeoff between the accuracy and the time consumption. Fig. 7(c) shows the statistical plots of the learning accuracy of SNN operated with different linearity and accuracy of all-optical synaptic devices, indicating that good learning accuracy and stability is achieved thanks to the improved synaptic behavior.

IV. Conclusion

In summary, with a specially designed structure of discrete GST islands on a directional coupler, we have obtained a novel all-optical synaptic device, which could realize both LTP and LTD functions at the same time. Photo-thermal coupling simulations demonstrate that the transition from the amorphous state to the crystalline state can be achieved one by one under the 'write' speed of sub-ns orders. Furthermore, by adjusting the size and position of the GST islands, we have achieved improvements in the linearity and accuracy of synaptic weights. Moreover, via the verification in SNN, this improvement can increase the recognition accuracy of written figures from the original 50% to 91%. With the recent advances in Photonic Neuromorphic, the proposed all-optical synaptic device based GST provides a more promising solution of the neural synaptic network.

References

[1] A. Sebastian, M. L. Gallo, R. Khaddam-Aljameh, and E. Eleftheriou, "Memory devices and applications for in-memory computing," *Nature Nanotechnol.,* vol. 15, no. 7, pp. 529–544, 2020.

[2] G. Indiveri and S. Liu, "Memory and information processing in neuromorphic systems," *Proc. IEEE*, 2015*,* vol. 103, no. 8, pp. 1379–1397.

[3] K. Roy, A. Jaiswal, and P. Panda, "Towards spike-based machine intelligence with neuromorphic computing," *Nature,* vol. 575, no. 7784, pp. 607–617, 2019.

[4] R. Athale and D. Psaltis, "Optical computing: Past and future," *Opt. Photon. News*, vol. 27, no. 6, pp. 32–39, 2016.

[5] T. Zhou *et al.*, "Large-scale neuromorphic optoelectronic computing with a reconfigurable diffractive processing unit," *Nature Photon.,* vol. 15, no. 5, pp. 367–373, 2021.

[6] C. Wu, H. Yu, S. Lee, R. Peng, I. Takeuchi, and M. Li, "Programmable phase-change metasurfaces on waveguides for multimode photonic convolutional neural network," *Nature Commun.,* vol. 12, no. 1, p. 96, 2021.

[7] M. Wuttig, H. Bhaskaran, and T. Taubner, "Phase-change materials for non-volatile photonic applications," *Nature Photon.,* vol. 11, no. 8, pp. 465–476 2017.

[8] Z. Yang and S. Ramanathan, "Breakthroughs in photonics 2014: Phase change materials for photonics," *IEEE Photon. J.,* vol. 7, no. 3, Jun. 2015, Art. no. 0700305.

[9] W. Zhang, R. Mazzarello, M. Wuttig, and E. Ma, "Designing crystallization in phase-change materials for universal memory and neuro-inspired computing," *Nature Rev. Mater.,* vol. 4, no. 3, pp. 150–168, 2019.

[10] A. Pirovano, A. L. Lacaita, F. Pellizzer, S. A. Kostylev, A. Benvenuti, and R. Bez, "Low-field amorphous state resistance and threshold voltage drift in chalcogenide materials," *IEEE Trans. Electron Devices,* vol. 51, no. 5, pp. 714–719, May 2004.

[11] Y. Zhang *et al.*, "Broadband transparent optical phase change materials for high-performance nonvolatile photonics," *Nature Commun.,* vol. 10, no. 1, Art. no. 4279, 2019.

[12] J. K. George *et al.*, "Neuromorphic photonics with electro-absorption modulators," *Opt. Exp.,* vol. 27, no. 4, pp. 5181–5191, 2019.

[13] J. Sun, E. Timurdogan, A. Yaacobi, E. S. Hosseini, and M. R. Watts, "Large-scale nanophotonic phased array," *Nature,* vol. 493, no. 7431, pp. 195–199, 2013.

[14] X. P. D. Y. Lei Yin, "Silicon-based optoelectronic synaptic devices," *Chin. Phys. B,* vol. 29, no. 7, pp. 70703–070703, 2020.

[15] A. N. Tait *et al.*, "Neuromorphic silicon photonics on foundry and cryogenic platforms," in *Proc. IEEE Photon. Soc. Summer Topical Meet. Ser.*, 2019, pp. 1–2.

[16] Y. Shen *et al.*, "Deep learning with coherent nanophotonic circuits," *Nature Photon.,* vol. 11, no. 7, pp. 441–446, 2017.

[17] H. Zhang *et al.*, "Electro-optical switch using Ge2Sb2Te5 phase-change material in a silicon MZI structure," in *Proc. Conf. Lasers Electro-Opt. Pacific Rim (CLEO-PR)*, 2017, pp. 1–3.

[18] H. Zhang, L. Zhou, J. Xu, L. Lu, J. Chen, and B. M. A. Rahman, "All-optical non-volatile tuning of an AMZI-coupled ring resonator with GST phase-change material," *Opt. Lett.,* vol. 43, no. 22, pp. 5539–5542, 2018.

[19] H. Zhang, L. Zhou, J. Xu, L. Lu, J. Chen, and B. M. A. Rahman, "Silicon microring resonators tuned with GST phase change material," in *Proc. Asia Commun. Photon. Conf. (ACP)*, 2018, pp. 1–3.

[20] Z. Hanyu, L. Zhou, J. Xu, L. Lu, and B. Rahman, "All-optical synapses based on silicon microring resonators actuated by the phase change material Ge2Sb2Te5," in *Proc. CLEO: Sci. Innovations*, 2019, p. STh4H.2.

[21] C. Ríos *et al.*, "Integrated all-photonic non-volatile multi-level memory," *Nature Photon.,* vol. 9, no. 11, pp. 725–732, 2015.

[22] I. Chakraborty, G. Saha, A. Sengupta, and K. Roy, "Toward fast neural computing using all-photonic phase change spiking neurons," *Sci. Rep.,* vol. 8, no. 1, 2018, Art. no. 12980.

[23] N. Wang, H. Zhang, L. Zhou, L. Lu, and B. Rahman, "Design of ultra-compact optical memristive switches with GST as the active material," *Micromachines,* vol. 10, no. 7, pp. 453–460, 2019.

[24] H. Zhang, L. Zhou, J. Xu, N. Wang, and H. Hu, "Nonvolatile waveguide transmission tuning with electrically-driven ultra-small GST phase-change material," *Sci. Bull.,* vol. 64, no. 11, pp. 782–789, 2019.

[25] Q. Zhang, Y. Zhang, J. Li, R. Soref, T. Gu, and J. Hu, "Broadband nonvolatile photonic switching based on optical phase change materials: Beyond the classical figure-of-merit," *Opt. Lett.,* vol. 43, no. 1, pp. 94–97, Jan. 1, 2018.

[26] S. Han, T. J. Seok, N. Quack, B.-W. Yoo, and M. C. Wu, "Large-scale silicon photonic switches with movable directional couplers," *Optica,* vol. 2, no. 4, pp. 370–375, 2015.

[27] P. Xu, J. Zheng, J. K. Doylend, and A. Majumdar, "Low-loss and broadband nonvolatile phase-change directional coupler switches," *ACS Photon.*, vol. 6, no. 2, pp. 553–557, 2019.

[28] J. Feldmann *et al.*, "Calculating with light using a chip-scale all-optical abacus," *Nature Commun.,* vol. 8, no. 1, 2017, Art. no. 1256, .

[29] J. Song, S. Ghosh, N. Dhingra, H. Zhang, L. Zhou, and B. M. A. Rahman, "Feasibility study of a Ge2Sb2Te5-clad silicon waveguide as a non-volatile optical on-off switch," *OSA Continuum,* vol. 2, no. 1, pp. 49–63, 2019.

[30] L. Zhou, H. Zhang, H. Hu, L. Lu, J. Chen, and B. M. A. Rahman, "Miniature silicon nanobeam resonator tuned by GST phase change material," in *Proc. Conf. Lasers Electro-Opt. Pacific Rim (CLEO-PR)*, 2018, pp. 1–2.

[31] K. Y. Hsiang *et al.*, "Ferroelectric hfzro2 with electrode engineering and stimulation schemes as symmetric analog synaptic weight element for deep neural network training," *IEEE Trans. Electron Devices,* vol. 67, no. 10, pp. 4201–4207, Oct. 2020.

[32] P. Chen, X. Peng, and S. Yu, "NeuroSim+: An integrated device-to-algorithm framework for benchmarking synaptic devices and array architectures," in *Proc. IEEE Int. Electron Devices Meet. (IEDM)*, 2017, pp. 6.1.1–6.1.4.

[33] P. Chen *et al.*, "Mitigating effects of non-ideal synaptic device characteristics for on-chip learning," in *Proc. IEEE/ACM Int. Conf. Comput.-Aided Des. (ICCAD)*, 2015, pp. 194–199.

[34] Z. Cheng, C. Ríos, W. H. P. Pernice, C. D. Wright, and H. Bhaskaran, "On-chip photonic synapse," *Sci. Adv.,* vol. 3, no. 9, Sep. 2017, Art. no. e1700160.

[35] H. Zhang *et al.*, "Ultracompact Si-GST hybrid waveguides for nonvolatile light wave manipulation," *IEEE Photon. J.,* vol. 10, no. 1, Feb. 2018, Art. no. 2200110.

[36] Comsol Multiphys. Reference Guide for COMSOL 5.6, [Online] Available: https://www.comsol.com

[37] J. Zheng *et al.*, "Nonvolatile electrically reconfigurable integrated photonic switch enabled by a silicon PIN diode heater," *Adv. Mater.,* vol. 32, no. 31, Art. no. 2001218, 2020. [Online] Available: https://doi.org/10.1002/adma.202001218

[38] Lumerical. Lumerical Inc. [Online]. Available: http://www.lumerical.com/tcad-products/fdtd/

[39] I. Chakraborty, D. Roy, and K. Roy, "Technology aware training in memristive neuromorphic systems for nonideal synaptic crossbars," *IEEE Trans. Emerg. Topics Comput. Intell.,* vol. 2, no. 5, pp. 335–344, Oct. 2018.